



### Ferroelectric Nematic Droplets in their Isotropic Melt

Journal:	<i>Soft Matter</i>
Manuscript ID	SM-COM-10-2022-001395.R1
Article Type:	Communication
Date Submitted by the Author:	29-Nov-2022
Complete List of Authors:	<p>Perera, Kelum; Kent State University, Liquid Crystal  Saha, Rony; Kent State University, Department of Physics  Nepal, Pawan; Kent State University, Department of Chemistry and  Biochemistry  Dharmarathna, Rohan; Kent State University, Liquid Crystal  Hosseini, Md Sakhawat; Kent State University, Advanced Materials and  Liquid Crystal Institute and Materials Science Graduate Program  Mostafa, Md; Kent State University, Liquid Crystal  Adaka, Alex; Kent State University, Liquid Crystal  Waroquet, Ronan; Kent State University, Liquid Crystal  Twieg, Robert; Kent State University, Department of Chemistry  Jakli, Antal; Kent State University, Liquid Crystal</p>

# Ferroelectric Nematic Droplets in their Isotropic Melt

*Kelum Perera<sup>1,2</sup>, Rony Saha<sup>1,2</sup>, Pawan Nepal<sup>4</sup>, Rohan Dharmarathna<sup>2</sup>, Md Sakhawat Hossain<sup>2,3</sup>,  
Md Mostafa<sup>2,3</sup>, Alex Adaka<sup>2,3</sup>, Ronan Waroquet<sup>2</sup>, Robert J. Twieg<sup>4</sup> and Antal Jákl<sup>1,2,3</sup>*

<sup>1</sup>Department of Physics, Kent State University, Kent OH, 44242, USA

<sup>2</sup>Advanced Materials and Liquid Crystal Institute, Kent State University, Kent OH, 44242, USA

<sup>3</sup>Materials Science Graduate Program, Kent State University, Kent OH, 44242, USA

<sup>4</sup>Department of Chemistry and Biochemistry, Kent State University, Kent, OH 44242, USA

## Abstract

The isotropic to ferroelectric nematic liquid transition had been theoretically studied over one hundred years ago, but its experimental studies are rare. Here we present experimental results and theoretical considerations of novel electromechanical effects of ferroelectric nematic liquid crystal droplets coexisting with the isotropic melt. We find that the droplets have flat pancake-like shapes that are thinner than the sample thickness as long as there is room to increase the lateral droplet size. In the center of the droplets a wing-shaped defect with low birefringence is present that moves perpendicular to a weak in-plane electric field, and then extends and splits in two at higher fields. Parallel to the defect motion and extension, the entire droplet drifts along the electric field with a speed that is independent of the size of the droplet and is proportional to the amplitude of the electric field. After the field is increased above  $1\text{mV}/\mu\text{m}$  the entire droplet gets deformed and oscillates with the field. These observations led us to determine the polarization field and revealed the presence of a pair of positive and negative bound electric charges due to divergences of polarization around the defect volume.

**Keywords:** *polarization rotation, Liquid crystals, circular domains,*

## 1. Introduction

The isotropic-nematic phase transition intrigued physicists in the early 20<sup>th</sup> century soon after the discovery of liquid crystals at the end of the 19<sup>th</sup> Century<sup>1,2</sup>. In 1916 Born proposed that nematic liquid crystals are ferroelectric in which the strong dipole–dipole interactions among molecules

stabilize the orientational order against thermal fluctuations<sup>3</sup>. The condition for the molecular dipole moment  $\mu$  can be estimated<sup>4</sup> to be  $\frac{\mu^2}{\epsilon_0 \epsilon V_m} > k_B T$ , where  $V_m$  is the molecular volume,  $k_B$  is Boltzmann constant and  $T$  is the temperature. At room temperature with  $V_m \sim 1 \text{ nm}^3$  and  $\epsilon \sim 10$ , predicting that the molecular dipoles must be larger than  $\mu \sim 6 \text{ Debye}$ . Experimentally, ferroelectric nematic fluids were found about a century after Born's paper by Nishikawa et al.<sup>5</sup> and Mandle et al.<sup>6,7</sup> in materials containing rod-shaped molecules with dipole moments of about  $10 \text{ Debye}$ . In these materials (called DIO and RM734, respectively) the ferroelectric phase did not form directly below the isotropic phase, but below an intervening non-ferroelectric nematic phase. These publications inspired many groups worldwide to study the nature of ferroelectric nematic ( $N_F$ ) phase of liquid crystals as summarized in a perspectives article by Sebastián et al.<sup>8</sup> The  $N_F$  phase with polar order<sup>9,10</sup> has unique viscoelasticity<sup>11</sup>, topology<sup>12,13</sup> and electrooptical properties<sup>14-16</sup> that may play a key role in many future technological advances like data storage, sensors, mechanical actuators, displays with sub-millisecond switching, and other optoelectronic applications<sup>15-17</sup>.

In the past five years many  $N_F$  materials have been synthesized but only a few were found to exhibit a direct isotropic to ferronematic transition<sup>18-20</sup>. In these materials the  $N_F$  phase forms via nucleation where polarized optical microscopy (POM) images revealed circular-shaped domains that were assumed to be spherical<sup>15</sup>. Second Harmonic Generation (SHG) interferometric microscopy studies on the  $N_F$  domains showed that tangential clockwise and anticlockwise directions of polarization structure with equal probability<sup>20</sup>. Such observations are consistent with polarimetric observations by Máthé et al. on  $N_F$  sessile droplets in air<sup>12</sup>. The concentric circular polarization patterns imply the existence of  $+1$  defects in the center of the domains<sup>20</sup>. On cooling in the  $Iso + N_F$  two phase range, the nuclei gradually grow from the isotropic liquid, merge, and eventually fill the whole area in a mosaic-like pattern in the  $N_F$  phase<sup>8,20</sup>.

In this paper, we present detailed studies of the  $N_F$  nuclei in various electric fields on a material with a direct  $Iso - N_F$  transition. We found that the initial spherical nuclei grow radially sideways to form pancake shapes that can float in the isotropic fluid. In external in-plane electric fields, the central defect lines move perpendicular to the electric field, while entire domains move along the applied field. Based on these observations we determine the polarization field and show the

presence of positive and negative bound electric charges due to divergences of polarization around the defect area.

## 2. Material and methods

The synthesis and chemical characterization of RT11064, Benzoic acid, 2,4-dimethoxy-, 3-fluoro-4-[(3-fluoro-4-nitrophenoxy)carbonyl]phenyl ester, is provided in the Supporting Information (SI) section. The molecular structure of RT11064 and the DSC curves at the third heating-cooling cycle is shown in Figure 1. RT11064 is identical to compound 3 of Reference<sup>21</sup>.

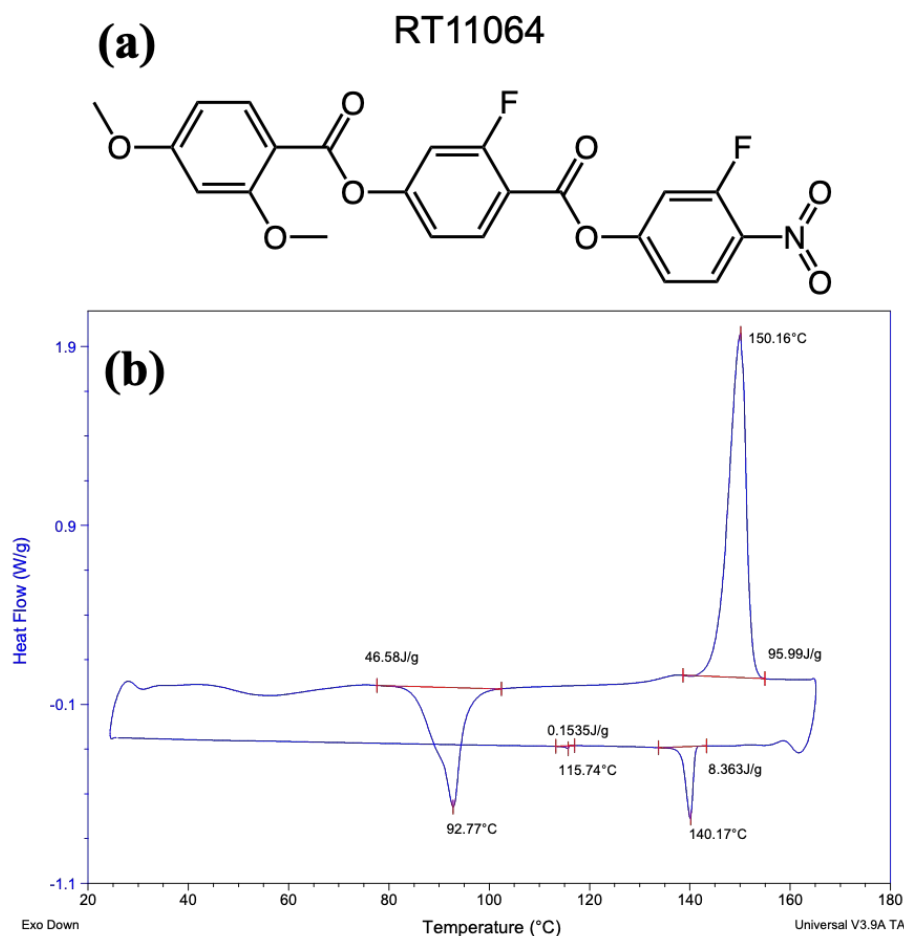


Figure 1: Molecular structure of RT11064 (a) and the DSC curves at the third heating-cooling cycle (heating and cooling rate = 5 °C/min. Sample size = 5.567 mg) indicating a phase sequence: Iso – 140°C – (Iso+N<sub>F</sub>) – 115°C N<sub>F</sub> – Cr (93°C).

For Polarized Optical Microscopy (POM) 5 – 10 μm thick samples were placed in an Instec HS200 heat stage and viewed through crossed polarizers with an Olympus BX60 microscope. Electro-optical and ferroelectric polarization measurements were carried out in cells with rubbed

PI-2555 polyamide coating and in one plate with two 2 mm wide conducting ITO strips separated by 1 mm distance. The cells were assembled using NOA68 glue with appropriate spacers to achieve uniform thickness. An HP 33120A function generator amplified by FLC F10A 20X amplifier from Instec was used to apply AC voltages.

For the polarization measurements, a 10  $\mu\text{m}$  thick sample was studied under 200 Hz triangular electric fields. Since the gap between the electrodes is much larger than the film thickness, we assume that the net polarization charge  $Q = P_o A$  appearing on the in-plane electrodes is independent of the size of the electrodes<sup>9</sup> and is determined only by the length of the electrodes multiplied by the film thickness ( $A = 1\text{cm} \times 10\mu\text{m} = 10^{-7} \text{m}^2$ ) normal to the polarization vector.

For the observation of the electromechanical effects, we applied triangular and rectangular waveforms from 100 mHz – 1.5 Hz with different amplitudes using HP 33120A function generator.

### 3. Experimental Results

Representative polarized optical microscopy (POM) textures of a 6  $\mu\text{m}$  cell are shown in Figure 2a on cooling from the isotropic phase with a rate of 1  $^\circ\text{C}/\text{min}$ . The  $N_F$  phase nucleates from the isotropic phase as circular-shaped domains. The radii of the very first domains are less than the film thickness, but then they grow laterally with radii exceeding the film thickness until they merge as shown in Figure 2a. The two-phase range was found to depend on the film thickness and cooling rate: the thicker is the film and slower is the cooling, the wider is the range. The birefringence color is almost temperature independent in the two-phase region, then abruptly increases once the domains merge to form the pure  $N_F$  phase where it is only slightly increasing on cooling. In the two-phase range (top part of Figure 2a) the optical path difference can be estimated from the Michel-Levy chart (see the top part of Figure 2b) to be about 1050 nm, whereas in the pure  $N_F$  phase it is about 1250 nm.

Assuming planar alignment, we estimate the birefringence in the  $N_F$  phase to be about  $1.25 \mu\text{m}/6 \mu\text{m} \sim 0.21$ , where the numerator is the optical path difference and the denominator is the film thickness. With the observed slightly smaller birefringence, we estimate the thickness of the  $N_F$  nuclei to be  $1.05 \mu\text{m}/0.20 \sim 5.2 \mu\text{m}$ , i.e., smaller than the film thickness. Illustration of the side-view of the  $N_F$  domains right after the first spherical nuclei appear, of the pancake-shaped

nuclei in the middle of the  $Iso + N_F$  two-phase range, and the fused  $N_F$  domains in the pure  $N_F$  range in the top, middle, and bottom sections of Figure 2c, respectively.

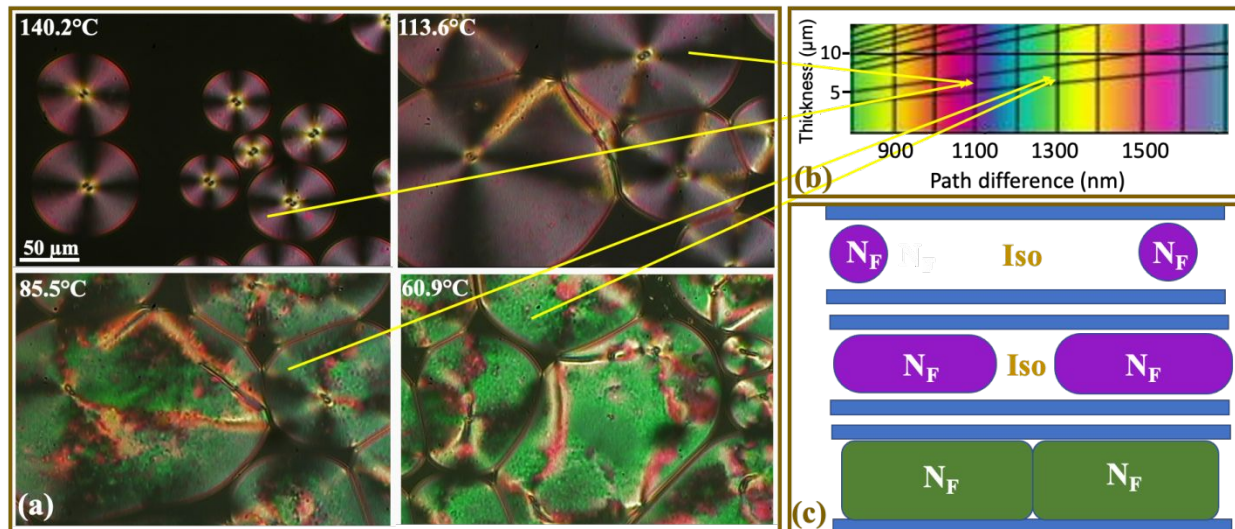


Figure 2: (a): Polarized Optical Microscopy (POM) images at 4 different temperatures of a 6 μm thick RT11064 film on cooling with 1 °C/min rate from the isotropic phase. (b): A portion of the Michel-Levi chart with the birefringence colors corresponding to the POM colors at different temperatures. (c): Illustration of the approximate cross-section of the phase structures in the  $Iso-N_F$  range and the  $N_F$  range, based on the POM images in (a).

The temperature dependence of the ferroelectric polarization of RT11064 with representative time dependences of the polarization current in the inset is shown in Figure 3. The 118°C-140°C temperature range corresponds to the two-phase range where the  $N_F$  volume of the nuclei increases. In the pure  $N_F$  range the polarization linearly increases from about 6.5 μC/cm<sup>2</sup> to 7.8 μC/cm<sup>2</sup>. The solid line indicates the temperature dependence of the ferroelectric polarization of the individual  $N_F$  nuclei in the two-phase range.

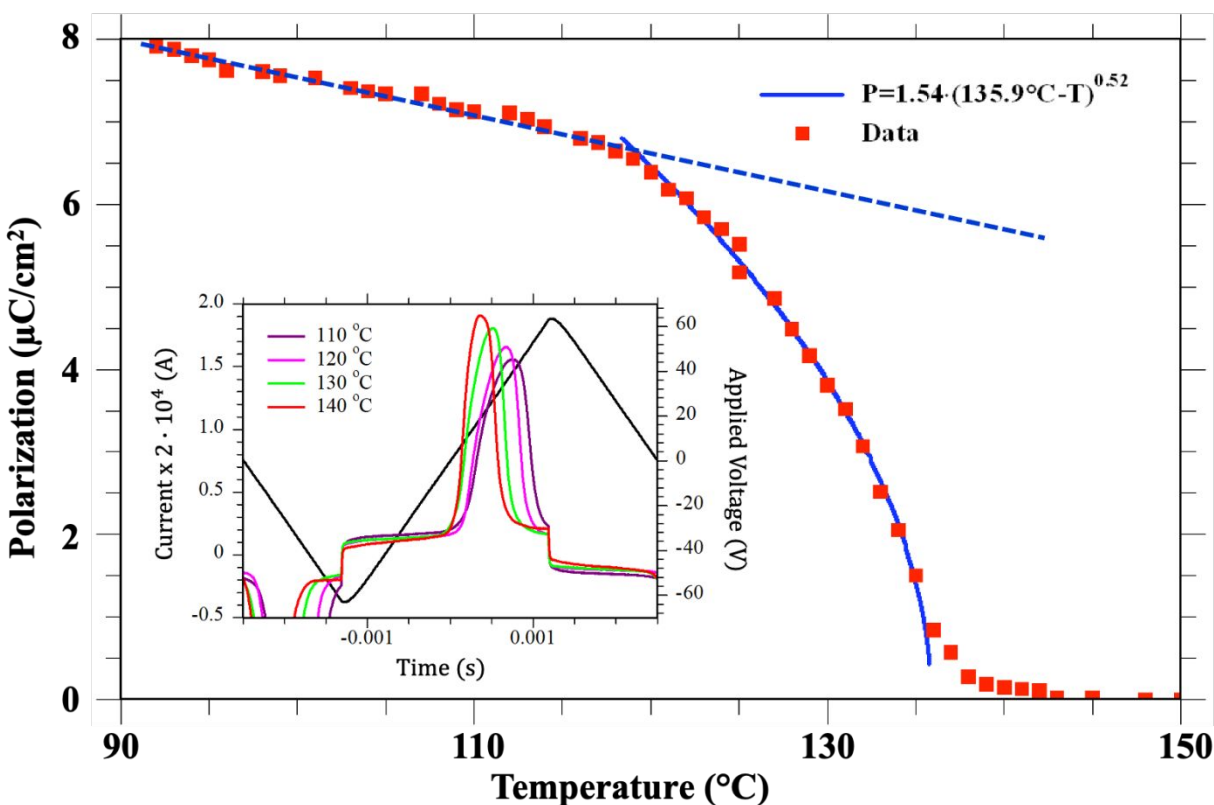


Figure 3: Temperature dependence of the spontaneous polarization of RT11064. Inset: Time dependence of the applied voltage (Right axis) and the measured voltage dropped on 20k $\Omega$  resistance (left axis) at selected temperatures

POM images of representative  $N_F$  nuclei in various electric fields are shown in Figure 4. Figure 4 (a and b) compare the structures and positions of two nuclei at zero electric field and 3 seconds after application of a 0.6 mV/ $\mu\text{m}$  electric field in the  $x$  direction. One can see two simultaneous motions. Initially, the central defect moves perpendicular to the electric field by a distance  $\Delta y \approx 10\mu\text{m}$  for the top  $D \approx 50\mu\text{m}$  diameter nucleus and by  $\Delta y \approx 7\mu\text{m}$  for the bottom  $D \approx 35\mu\text{m}$  diameter nucleus. At the same time both nuclei move along the electric field by approximately the same  $\Delta x \approx 16\mu\text{m}$  distance. While all droplets moved in the same direction, the defect in the center of each domain moved perpendicular to the electric field either left or right as shown in Figure 4b. The velocity of the droplets is found to be independent of the rubbing direction, which indicates that these droplets do not touch the substrates. Under weak DC voltages, all droplets were found to move in the electric field toward the negative electrodes.

Figure 4c shows a  $D \approx 90\mu\text{m}$  diameter circular shaped nucleus at zero,  $0.4\text{ mV}/\mu\text{m}$  and  $0.6\text{ mV}/\mu\text{m}$  electric fields from top to bottom in  $d = 5.5\text{ }\mu\text{m}$  thick film between crossed polarizers. The directions of the crossed polarizers are indicated by white arrows. We see the nucleus has second-order magenta color outside the defect area, black in the defect, and first-order whitish to second-order green colors around the defect. Compared with the Michel-Levy chart, we see that the magenta color corresponds to an optical path difference of  $\Gamma = \Delta n \cdot d \approx 1.1\text{ }\mu\text{m}$ . From the  $d = 5.5\text{ }\mu\text{m}$  film thickness this provides that the birefringence of the  $N_F$  nucleus is  $\Delta n \approx 0.2$ , which agrees with the estimate based on the POM images in Figure 2a. In the defect, the dark area indicates zero birefringences, and the whitish (green) color corresponds to  $\Delta n \sim 0.05$  ( $\Delta n \sim 0.13$ ) birefringence.

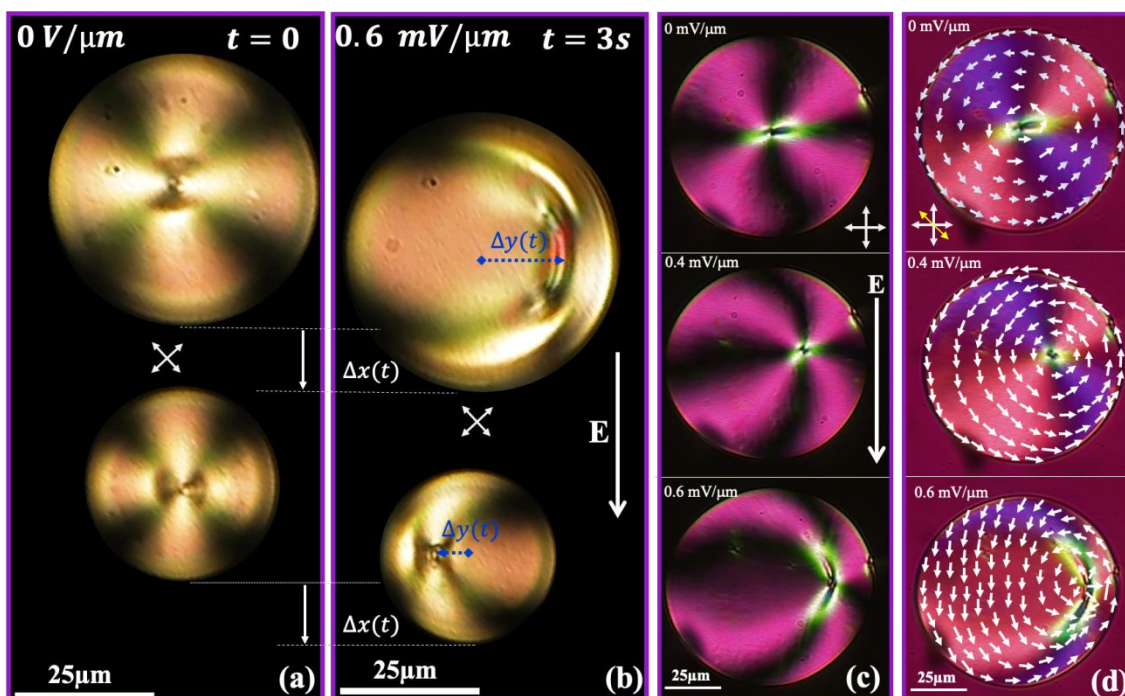


Figure 4: POM images of  $N_F$  nuclei formed at the  $Iso - N_F$  transition without and with an electric field applied in the  $x$  direction. (a): Two different-size nuclei in a  $10\text{ }\mu\text{m}$  thick film between crossed polarizers which are shown by crossed white double headed arrows. (b): The same nuclei as shown in (a), at  $t = 3\text{ s}$  after  $E = 0.6\text{ mV}/\mu\text{m}$  DC electric field was applied in  $x$  direction. (c): One  $90\text{ }\mu\text{m}$  diameter circular-shaped nucleus at zero,  $0.4\text{ mV}/\mu\text{m}$  and  $0.6\text{ mV}/\mu\text{m}$  electric fields from top to bottom in  $5.5\text{ }\mu\text{m}$  thick film between crossed polarizers. (d): The same nucleus as in (c) but now a  $\lambda = 530\text{ }\mu\text{m}$  waveplate with slow axis inserted at  $45^\circ$  with respect to the vertical polarizer. White arrows indicate the approximate ferroelectric polarization directions.

As shown by yellow double headed arrow, Figure 4d shows the same nucleus at the same fields as in Figure 4c but now with a  $\lambda = 530\text{ }\mu\text{m}$  waveplate inserted with the slow axis making  $45^\circ$  with

respect to the vertical polarizer placed above the sample. When the optical axis of the LC is parallel to that of the waveplate, the resulting optical path difference far from the defects is  $\Gamma_{\parallel} \approx (1100 + 530)\text{nm} = 1630\text{ nm}$  corresponding to third-order light pink color. When the director of the LC is perpendicular to that of the waveplate, then  $\Gamma_{\perp} \approx (1100 - 530)\text{ nm} = 570\text{ nm}$  corresponding to a second-order purple color. From these observations, we can verify that, except for near the defect area, the director has tangential distribution in agreement with<sup>11,15,12</sup>. As we will discuss later, combining this information with the direction of the movement of the defect, we can also determine the direction of the polarization (see white arrows overlaid the POM images in Figure 4d), as it is reasonable to assume that the field will deform the structure to provide a net polarization along the electric field. The change of colors around the defect area (whitish to green and from green to yellow) is also consistent with the previous conclusion that the alignment is homeotropic with zero birefringences in the core of the defect and the birefringence increasing slowly in one direction (along the wing), slowly (within  $20\ \mu\text{m}$ ), and abruptly (within  $<3\ \mu\text{m}$ ) perpendicular to it. This trend indicates anisotropic tilt variation around the defect.

The voltage dependence of the amplitude of the side-wise motion of the defect for a  $46\ \mu\text{m}$  diameter nucleus at  $4^{\circ}\text{C}$  below the appearance of the first nucleus measured in a  $5\ \mu\text{m}$  cell is shown in Figure 5a at various frequencies between 500 mHz and 1 Hz. One can see that up to  $1\text{V}$  ( $E < 1\ \text{mV}/\mu\text{m}$ ) the amplitude is proportional to the applied in-plane voltage. The top insets show that the motion follows well the sinusoidal variation of the applied voltage, while the lower inset illustrates the direction of the displacement with respect to the externally applied field.

The motion of the droplets along the electric field is demonstrated in Supporting Video 1. The electric field dependence of the velocity of a  $D = 78\ \mu\text{m}$  diameter droplet under a square wave electric field is shown in Figure 5b for several frequencies. The inset at the top right corner of the figure shows that for 100 mHz square wave voltage the velocity is constant while the voltage is constant. The main pane of the figure shows that the velocity is proportional to the applied electric field and decreases at increasing frequencies. The frequency dependence in 0 – 2.6 Hz interval of  $1\ \text{mV}/\mu\text{m}$  electric field is shown in the top-left inset with the fitting equation  $v = 3 + 7.4 \cdot e^{-\frac{f}{0.47}}$  where  $f$  is the applied frequency. This indicates an exponential decay of the velocity from  $10.4\ \mu\text{m}/\text{s}$  speed at DC field to  $\approx 3\ \mu\text{m}/\text{s}$  at high ( $f \gg 1\ \text{Hz}$ ) frequencies. The 0.47 Hz in the exponent gives the relaxation frequency.

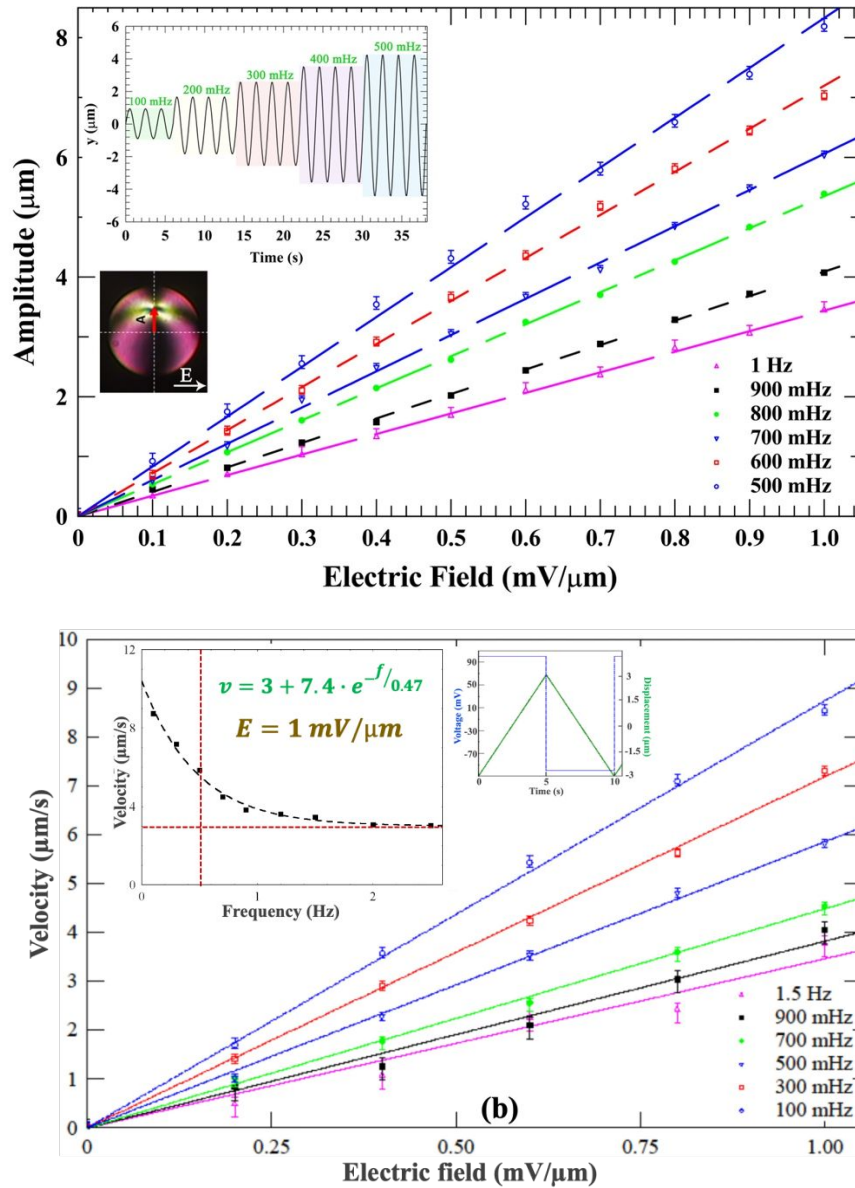
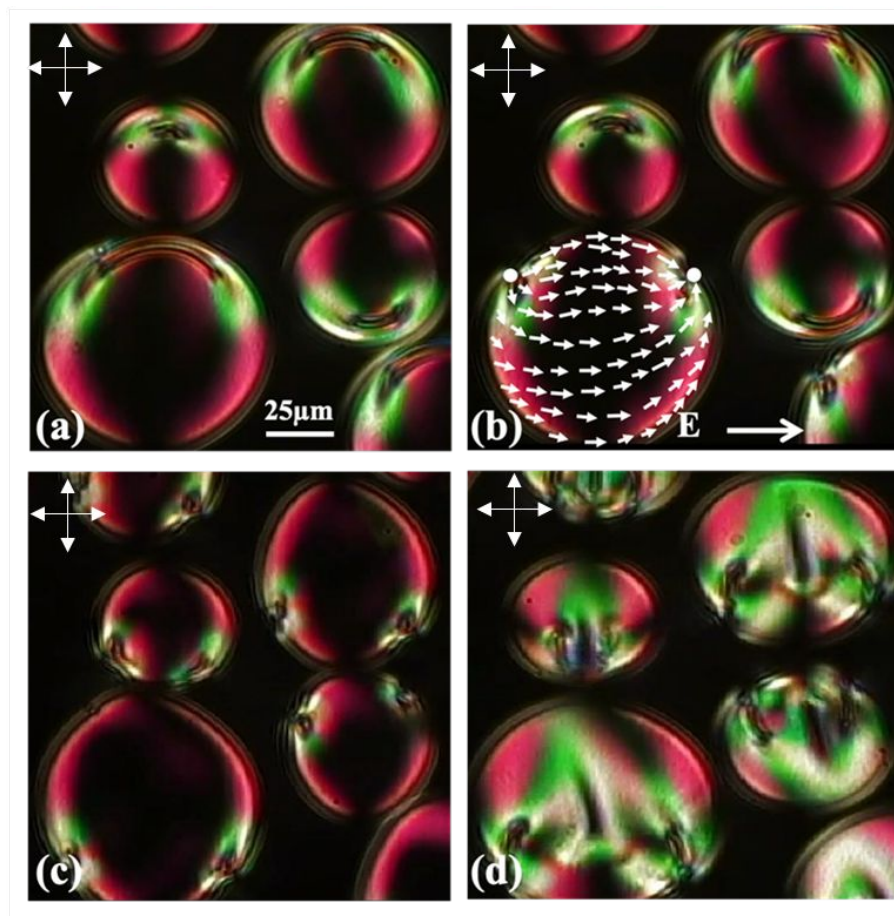


Figure 5: Electric field dependence of the defect movement and the velocity of the  $N_F$  droplets. (a): Electric field dependence of the displacement of the central defect of a  $D = 46 \mu\text{m}$  diameter droplet in  $d = 5 \mu\text{m}$  thick film at  $4^\circ\text{C}$  below the appearance of the first nucleus in the isotropic phase. Top-left inset shows the sinusoidal time dependence of the displacement at several frequencies. The lower inset illustrates the direction of the displacement with respect to the externally applied field (b): Electric field dependence of the velocity of a  $D = 78 \mu\text{m}$  diameter  $N_F$  nucleus for various square wave fields. Top right inset: displacement under 100 mHz square wave voltage. Top-left inset: Frequency dependence of the velocity in 0 – 2.6 Hz interval at  $1 \text{ mV}/\mu\text{m}$  electric field with the fitting equation.

All the above measurements were done at low fields ( $E < 1 \text{ mV}/\mu\text{m}$  or  $f > 0.5 \text{ Hz}$ ). At increasing fields and/or decreasing frequencies, the defects not only move inside the droplets, but they extend and split and simultaneously even the shapes of the droplets change.



*Figure 6: Illustration of the behavior of the pancake-like droplets in high electric fields applied horizontally. (a and b):  $f = 0.1 \text{ Hz}$  with a maximum amplitude  $E_m = 0.5 \text{ mV}/\mu\text{m}$  (a) snapshot when  $E = 0.4 \text{ mV}/\mu\text{m}$ ; (b) snapshot at  $E = 0.5 \text{ mV}/\mu\text{m}$ . (c and d):  $f = 0.1 \text{ Hz}$   $E_m = 1.5 \text{ mV}/\mu\text{m}$ ; (c)  $E = 0.5 \text{ mV}/\mu\text{m}$ ; (d)  $E = 1.5 \text{ mV}/\mu\text{m}$ . Crossed polarizers are in horizontal and vertical directions as shown by white double headed arrows.*

The extension and the split of the defects along the applied field are shown in Figure 6 (a and b) when  $f = 0.1 \text{ Hz}$  field is applied with  $E_m = 0.5 \text{ mV}/\mu\text{m}$  amplitude. Figure 6a shows the extension of the defect at  $E \sim 0.4 \text{ mV}/\mu\text{m}$  field. Figure 6b shows a snapshot at  $E = 0.5 \text{ mV}/\mu\text{m}$  after the defect has split into two and situated at the opposite sides of the droplets. The approximate polarization field is overlaid on one of the droplets. Upon increasing amplitude of the field, the droplet shape changes as shown for  $f = 0.1 \text{ Hz}$  in Figure 6(c and d) and in Supporting Video 2. First the droplets elongate along the motion of the defect forming an oblate ellipsoid and reach

their highest aspect ratio right after the defect splits, as shown in Figure 6c at  $E = 0.5 \text{ mV}/\mu\text{m}$ . Further increasing fields, the droplets start extending along the applied field forming a prolate ellipsoid, and reach their highest aspect ratio at the highest applied field, as shown in Figure 6d at  $E = 1.5 \text{ mV}/\mu\text{m}$ . As it is apparent from the pictures of the different droplets in Figure 6, the magnitude of the fields where the above changes appear, depends also on the size of the droplets: the smaller is the droplets, the higher is the required field for the above changes. The threshold fields also increase with increasing frequencies (for example, the threshold for splitting increases to 7 V at 0.7 Hz).

#### 4. Discussion

The results we presented above, reveal several notable properties of the ferroelectric nematic liquid crystal droplets that coexist with the isotropic liquid phase. (i) The droplets have a flat pancake-like shape that is thinner than the sample thickness, if there is room to increase the droplets laterally. (ii) In the center of the droplets, a defect with a wing shape darker pattern appears instead of the four Maltese crosses that are seen far away from the central defect. (iii) In the presence of in-plane electric fields, the central defect moves perpendicular to the electric field, then extends along the field and at a high enough field it splits into two defects. (iv) While decreasing the field after strong and low-frequency fields are applied, the circular base extends along the field. (v) In parallel to the defect motion and extension, the entire droplet drifts along the electric field with a size-independent speed that is proportional to the in-plane electric field.

What follows, we attempt to explain all the above features starting with (ii) which is needed to explain (i) and all other features.

##### A. Polarization structure and shape of $N_F$ droplets

As in  $N_F$   $\hat{n} \neq -\hat{n}$ , one cannot have half-integer defects, which are the most stable in conventional nematics. The central defect therefore must have a strength of an integer number. As previous results on  $N_F$  droplets in an isotropic melt<sup>18-20</sup> and air<sup>12</sup> showed, the director and the polarization have tangential distribution far away from the central defect. Therefore, it is reasonable to assume a simple +1 central defect line as proposed by Li et al<sup>20</sup>. Such a structure however would result in a simple 4 brush Maltese cross along the crossed polarizers. This is not

true in our case as shown in Figure 2 and Figure 4a, where two-fold wing-type structures are seen. We propose this structure can be explained by the director and polarization field we show in Figure.

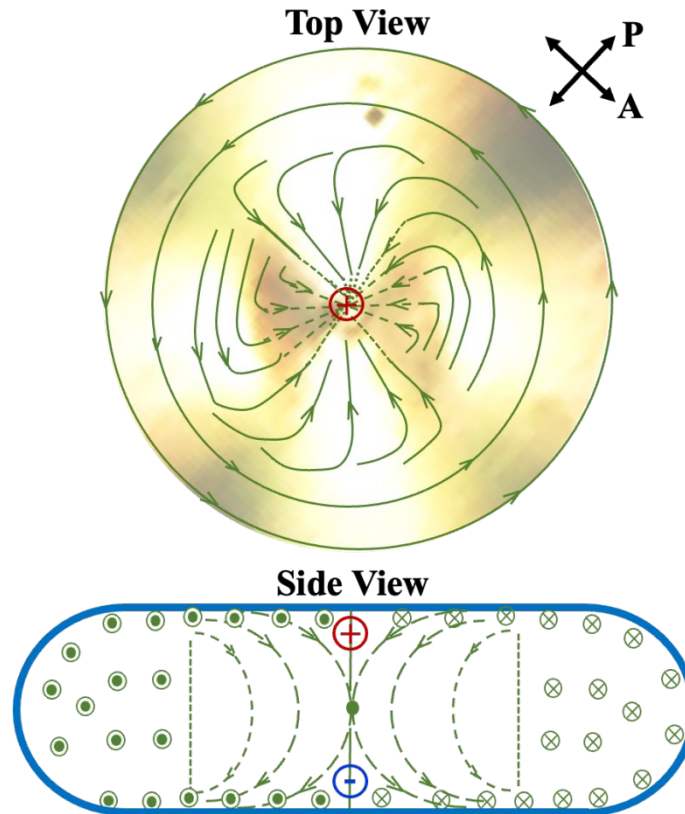


*Figure 7: Illustration of the director structure in the pancake-like  $N_F$  domains. In the top view, the director structure is drawn on the POM image of a part of an actual droplet shown in Figure 4a. Dotted lines indicate the director tilting away from the plane of the drawing. Shorter dots mean larger tilt. A dot (cross) in a circle shows the director perpendicular to the plane with polarization direction pointing toward (away) from the reader.*

The wing-type darker spots indicate an increasing deviation of the director field from the planar orientation toward the center. This leads to a  $+1$  point defect in the middle of a  $+1$  line defect running across the film, as seen in the side view of the droplet. Due to the divergence of the electric polarization, such a structure will lead to a bound charge density  $\rho = -\vec{\nabla} \cdot \vec{P}$ . Notably, the divergence at the upper and lower parts are opposite (in the example shown in Figure 7, it is inward in the upper part and outward in the bottom) leading to different signs of bound charges at the upper and lower parts (e.g., the positive charge in the upper and negative charge in the lower part in Figure 7). This funnel-like polarization divergence appears to have two-fold symmetry where the inward polarization divergence is concentrated along the East-West direction as in the top

droplet of Figure 4a, or can be along the South-North direction, as in the bottom droplet of Figure 4a. The situation corresponding to the former shown overlaid on the inner part of the POM of the top droplet of Figure 4a, is shown in the Top view of Figure 7.

The opposite bond charges at the upper and lower parts of the droplet attract free ions with opposite signs of the isotropic liquid above and below the droplets. The screening of the bound charges, therefore, requires the presence of the isotropic liquid below and above the  $N_F$  droplets, which may explain that the height of the  $N_F$  droplets is smaller than of the film thickness and, leading to a lateral growth and pancake shape of the droplets.

### B. Electric field induced defect motion

The lateral motion of the central defect under weak electric fields inside the pancake-shaped  $N_F$  domains perpendicular to the applied voltage can be understood by the field-induced polarization  $P_E$ , as schematically illustrated in Figure 4d. At zero field the polarization vector symmetrically circulates around the central defect line and the average polarization is zero. For weak fields with small displacement  $x$ , ( $x \ll R$ , where  $R$  is the radius of the droplet) the lateral length where the polarization points along the field is  $R + x$ , and the length where it points against the field is  $R - x$ , so the net polarization is proportional to  $x$ . For an order of magnitude approximation, the induced net polarization can be approximated as  $P_E \approx P_o \frac{x \cdot R}{R^2 \pi} = P_o \frac{x}{R \pi}$ . This will decrease the free energy of the ferroelectric domains by  $\Delta W \approx -P_o \frac{x}{R \pi} E \cdot w \cdot R^2 \pi = -P_o x R w E$ , where  $w$  is the height of the disc shaped ferroelectric domain, and  $E = \frac{V}{L}$  is the electric field due to the voltage  $V$  applied across the in-plane electrodes with a gap of  $L$ . The resulting force,  $F_E$  acting on the defect perpendicular in the field is  $F_E = -\frac{dW}{dx} \sim P_o R w E$ . This force is balanced by the drag force  $F_D$  acting on the defect line and the rotational viscous force  $F_\gamma$  related to the rotation of the polarization in an area of  $x \cdot 2R$ . The drag force can be given as  $F_D \sim \xi a \eta v$ , where  $a$  is the radius of the defect line,  $\eta$  is the relevant flow viscosity of the ferroelectric fluid and  $\xi(a, w, R)$  is a geometric factor depending on the size and shape of the defect line and the size of the disc-shaped domain. (Note: According to Stokes law, for spherical defects in an isotropic and infinite fluid,  $\xi = 6\pi$ .) The rotational viscous force can be approximated as  $F_\gamma \sim \frac{d}{dx} (2R w x \gamma_1 \dot{\phi})$ , where  $\gamma_1$  is the

rotational viscosity, and  $\dot{\varphi} = \frac{d\varphi}{dt} = 2\pi/T$ , where  $T$  is the time with speed  $v$  to translate by  $R$  ( $v = \frac{R}{T}$ , i.e.,  $\dot{\varphi} = \frac{2\pi v}{R}$ ). Accordingly, we can write that  $F_\gamma \approx 4\pi w\gamma_1 v$ . In equilibrium  $F_E = F_D + F_\gamma$ , i.e.,  $P_o R w E \approx v(\xi a \eta + 4\pi w\gamma_1)$ . This gives the order of magnitude approximation for the speed of the sidewise motion of the defect line as

$$v \sim \frac{P_o R w E}{\xi a \eta + 4\pi w\gamma_1}. \quad (1)$$

Experimentally we indeed see that the speed is proportional to weak applied field, and the maximum displacement  $x_m = v \cdot (T/4)$  relative to the radius of the disc shape domains  $\frac{x_m}{R}$  is constant as seen in Supplemental Video 3 [Different droplets size AC sine wave.mp4]. For a quantitative comparison with the experiment, from Figure 5a we take that at frequency  $f = 1$  Hz ( $T = 1$  s) and  $E = 1$  mV/ $\mu$ m,  $x_m \sim 4$   $\mu$ m. The polarization of the droplets can be extrapolated (see the solid blue line of Figure 3) to be  $P_o \sim 5 \cdot 10^{-2}$  C/m<sup>2</sup>. Taking  $w \sim 4$   $\mu$ m,  $a \sim 10$   $\mu$ m,  $R = 23$   $\mu$ m and  $\xi \sim 6\pi$ , and  $\eta \sim \gamma_1 \sim 0.2$  Pas, we get the right order of magnitude for the displacement for which are reasonable values for ferroelectric nematic liquid crystals<sup>11</sup>. We note that the direction of the movement of the defect in different domains can be opposite, because the direction of the *curl*  $\vec{P}$  can be opposite.

The elongation and separation of the defects along the increasing electric fields indicate that they have opposite bound charges  $\rho = -\nabla \cdot \vec{P}$  towards the opposite substrates. They are forced to move in the opposite direction along the external field, as we indeed observed experimentally (see Figure 4a,b). The separation of the bound charges involves the formation of a defect wall, as discussed by Lavrentovich<sup>4</sup>. We find that the charges split at a threshold field  $E_s \sim 0.4$  mV/ $\mu$ m when their separation  $s$  is  $s \sim 30$   $\mu$ m (see Figure ). From the balance of the electrostatic forces  $qE_s = K \frac{q^2}{s^2}$ , where  $K = 9 \cdot 10^9 \frac{\text{Nm}^2}{\text{C}^2}$  is the Coulomb constant, we get that  $q \cong 4 \cdot 10^{-17}$  C. Such value is much smaller than what we could expect from the divergence of the  $|q| = \int \nabla P \cdot dV_d \sim \frac{2P}{w} w A_d \sim 2P A_d$ , where  $V_d$  is volume of the defect, and  $A_d$  is the area of the defect. Assuming a defect area  $A_d \sim 10 - 100$   $\mu$ m<sup>2</sup> and  $P_o \sim 5 \cdot 10^{-2}$  C/m<sup>2</sup>, we expect  $q \sim 10^{-12} - 10^{-11}$  C. This indicates that most of the bound charges are screened out by free ions in the ferroelectric nematic fluid.

### C. Electric field induced shape change of the droplets

The force due to the interfacial tension  $\gamma_{I-N_F}$ , which is typically an order of magnitude smaller than the surface tension at air<sup>22</sup>  $\gamma_a \sim 3 \cdot 10^{-2} \text{J/m}^2$ , can be approximated as  $F_i \approx \gamma_{I-N_F} \cdot 2\pi R \sim 3 \cdot 10^{-3} \cdot 6\pi \cdot 10^{-5} \sim 6 \cdot 10^{-7} \text{N}$ . This is much greater than the electrostatic force,  $F_E = E \cdot q \cong 10^3 \cdot 4 \cdot 10^{-17} \text{N}$  arising from the separation of the polarization charges. This indicates that the deformation of the droplet shape is not related to the electrostatic force between the polarization charges. Rather, the deformation of the droplet shape should be the result of the ferroelectric interaction. Indeed, for  $P_o \sim 5 \cdot 10^{-2} \text{C/m}^2$  and  $E \sim 10^3 \text{V/m}$  the ferroelectric energy density is  $P_o E \sim 50 \text{Jm}^{-3}$ , which overcomes the interfacial energy density  $\frac{\gamma_{I-N_F}}{2R} < 3 \cdot 10^{-3} / 6 \cdot 10^{-5} = 50 \text{Jm}^{-3}$  for  $R \geq 30 \mu\text{m}$ . This is in agreement with our observations where for  $E < 1 \text{mV}/\mu\text{m}$ , we see deformation only for  $R \geq 30 \mu\text{m}$  droplets (see Figure ).

#### D. Electric field induced motion of the droplets

What remains to be explained is the movement of the droplets along the electric field. As we see in Figure 5b, the speed is independent of the size of the droplets, proportional to the electric field, and decreases at increasing frequencies (see inset to Figure 5b). These properties are typical of the electrophoresis of colloid particles in isotropic electrolytes<sup>23,24</sup>. For particles (like our droplets) where  $\frac{R}{\lambda_D} \gg 1$ , where  $\lambda_D$  is the Debye screening length, the resulting electrophoretic velocity is given by the Helmholtz-Smoluchovski equation<sup>23-25</sup>  $\vec{v}_{EP} = \frac{\varepsilon \cdot \varepsilon_0 \zeta}{\eta_{iso}} \vec{E}$ , where  $\varepsilon_0 = 8.854 \cdot 10^{-12} \frac{\text{C}^2}{\text{J} \cdot \text{m}}$  is the permittivity of the vacuum and  $\zeta$  is the Zeta potential, which is equal to the electric potential at the slip surface near the colloid particles. According to our experimental results shown in the inset of Figure 5b, the velocity decreases from about  $10 \mu\text{m/s}$  at  $0.1 \text{Hz}$  to about  $3 \mu\text{m/s}$  at  $2 \text{Hz}$ . For typical zeta potential of  $\zeta \sim 100 \text{mV}$ ,  $\eta_{iso} \sim 0.1 \text{Pas}$  and for  $E = 10^3 \text{mV}/\mu\text{m}$ , these velocity values require that the dielectric constant of the isotropic fluid be  $300 < \varepsilon < 1000$ . Such values were indeed observed in the isotropic melt of several ferroelectric nematic materials<sup>8</sup>. The observed relaxation frequency of  $f_c = 0.47 \text{Hz}$  (see fit to the inset in Figure 5b), can be explained by the screening of free charges around the  $N_F$  droplets. Indeed, for  $\frac{w}{\lambda_D} \gg 1$ , the relaxation frequency is related to the diffusion constant  $D_{iso} \sim 2 \cdot 10^{-11} \frac{\text{m}^2}{\text{s}}$  in the isotropic liquid and the

height of  $w \sim 4 \mu\text{m}$  of the  $N_F$  droplet as  $f_c \sim \frac{D_{iso}}{w^2} \sim 1 \text{ Hz}$ <sup>26</sup>, which is close to the observed relaxation frequency.

To summarize, we have studied ferroelectric nematic liquid crystal droplets coexisting with the isotropic melt. We have found that the droplets have flat pancake-like shapes that are floating in the isotropic melt. These droplets show two novel electromechanical effects. (i) In the center of the droplets, there is a defect with a low birefringence wing shape that moves perpendicular to a weak in-plane electric field, then it extends and splits in two at higher fields. (ii) In parallel to the defect motion and extension, the entire droplet drifts along the electric field with a speed that is independent of the size of the droplet and is proportional to the amplitude of the electric field. Finally, we found that at low frequencies  $< 0.5 \text{ Hz}$  above  $1 \text{ mV}/\mu\text{m}$  fields, the shape of the droplets gets deformed and oscillates between prolate and oblate ellipsoids related to the interfacial tension between the  $N_F$  droplets and the isotropic melt. These observations have led us to determine the polarization field and revealed the presence of a pair of positive and negative bound electric charges due to divergences of polarization around the defect volume.

## 5. Acknowledgment

This work was supported by NSF DMR 2210083.

## 6. References

- 1 F. Reinitzer, *Monatshfte für Chemie und verwandte Teile anderer Wissenschaften*, 1888, **9**, 421–441.
- 2 O. Lehmann, *Ann. der Phys. und Chemie*, 1891, **1**, 516–532.
- 3 M. Born, *Sitzungsber. Preuss. Akad. Wiss.*, 1916, **30**, 614–650.
- 4 O. D. Lavrentovich, *Proc. Natl. Acad. Sci. U. S. A.*, 2020, **117**, 14629–14631.
- 5 H. Nishikawa, K. Shiroshita, H. Higuchi, Y. Okumura, Y. Haseba, S. I. Yamamoto, K. Sago and H. Kikuchi, *Adv. Mater.*, 2017, **29**, 1702354.
- 6 R. J. Mandle, S. J. Cowling and J. W. Goodby, *Phys. Chem. Chem. Phys.*, 2017, **19**, 11429–11435.
- 7 R. J. Mandle, S. J. Cowling and J. W. Goodby, *Chem. - A Eur. J.*, 2017, **23**, 14554–14562.
- 8 N. Sebastián, M. Čopič, A. Mertelj and J. Stefan, *Phys. Rev. E*, 2022, **106**, 021001.
- 9 X. Chen, E. Korblova, D. Dong, X. Wei, R. Shao, L. Radzihovsky, M. A. Glaser, J. E.

- MacLennan, D. Bedrov, D. M. Walba and N. A. Clark, *Proc. Natl. Acad. Sci. U. S. A.*, 2020, **117**, 14021–14031.
- 10 J. Etxebarria, C. L. Folcia and J. Ortega, *Liq. Cryst.*, 2022.
- 11 R. Saha, P. Nepal, C. Feng, M. S. Hossain, M. Fukuto, R. Li, J. T. Gleeson, S. Sprunt, R. J. Twieg and A. Jákli, *Liq. Cryst.*, 2022, **49**, 1784–1796.
- 12 M. T. Máthé, Á. Buka, A. Jákli and P. Salamon, *Phys Rev E*, 2022, **105**, L052701.
- 13 B. Basnet, M. Rajabi, H. Wang, P. Kumari, K. Thapa, S. Paul, M. O. Lavrentovich and O. D. Lavrentovich, *Nat. Commun.*, 2022, **3**, 3932.
- 14 H. Nishikawa and F. Araoka, *Adv. Mater.*, 2021, **33**, 1–9.
- 15 C. Feng, R. Saha, E. Korblova, D. Walba, S. N. Sprunt and A. Jákli, *Adv. Opt. Mater.*, 2021, 2101230.
- 16 J. Li, H. Nishikawa, J. Kougo, J. Zhou, S. Dai, W. Tang, X. Zhao, Y. Hisai, M. Huang and S. Aya, 2020.
- 17 X. Chen, E. Korblova, M. A. Glaser, J. E. MacLennan, D. M. Walba and N. A. Clark, *Proc. Natl. Acad. Sci. U. S. A.*, 2021, 118.
- 18 A. Manabe, M. Bremer and M. Kraska, *Liq. Cryst.*, 2021, **48**, 1079–1086.
- 19 J. Li, Z. Wang, M. Deng, Y. Zhu, X. Zhang, R. Xia, Y. Song, Y. Hisai, S. Aya and M. Huang, *Giant*, 2022, **11**, 100109.
- 20 J. Li, R. Xia, H. Xu, J. Yang, X. Zhang, J. Kougo, H. Lei, S. Dai, H. Huang, G. Zhang, F. Cen, Y. Jiang, S. Aya and M. Huang, *J. Am. Chem. Soc.*, 2021, **143**, 17857–17861.
- 21 S. Brown, E. Cruickshank, J. M. D. Storey, C. T. Imrie, D. Pocięcha, M. Majewska, A. Makal and E. Gorecka, *ChemPhysChem*, 2021, **22**, 2506–2510.
- 22 C. Carboni, S. Al-Ruzaiqi, A. Al-Siyabi, S. Al-Harhi, A. K. George and T. J. Sluckin, *Mol. Cryst. Liq. Cryst.*, 2008, **494**, 114–126.
- 23 J. L. Anderson, *COLLOID TRANSPORT BY INTERFACIAL FORCES*, 1989, vol. 21.
- 24 O. D. Lavrentovich, *Ser. Condens. Matter Vol. 7 - Liq. Cryst. with Nano Microparticles*, *World Sci.*, 2016, 415–457.
- 25 A. V. Delgado, F. González-Caballero, R. J. Hunter, L. K. Koopal and J. Lyklema, *J. Colloid Interface Sci.*, 2007, **309**, 194–224.
- 26 A. Jákli and A. Saupe, *One and Two Dimensional Fluids – Physical Properties of Smectic Lamellar and Columnar Liquid Crystals*, Taylor and Francis, Boca Raton, 2006.

